Adaptive gold/vanadium dioxide periodic arrays for infrared optical modulation

Adrian-Ionut Bercea, Corinne Champeaux, Alexandre Boulle, Catalin Constantinescu, Julie Cornette, Maggy Colas, Sylvain Vedraine, Frédéric Dumas-Bouchiat

Adaptive gold/vanadium dioxide periodic arrays for infrared optical modulation

Adrian Ionut Bercea[1], Corinne Champeaux[1], Alexandre Boulle[1], Catalin Daniel Constantinescu[1], Julie Cornette[1], Maggy Colas[1], Sylvain Vedraine[2], Frédéric Dumas-Bouchiat[1]**

[1] Université de Limoges, CNRS, IRCER, UMR 7315, Limoges, F-87000, France
[2] Université de Limoges, CNRS, XLIM, UMR 7252, Limoges, F-87000, France

Corresponding e-mail addresses: adrian.bercea@unilim.fr and frederic.dumas-bouchiat@unilim.fr

Keywords:
Gold/vanadium dioxide nano-composite thin films
Localized surface plasmon resonance
Gold nanoparticles arrays
Solid state de-wetting

Abstract

Localized surface plasmon resonances (LSPR) make systems capable of concentrating and amplifying light intensity at their near surface. Applications ranging from energy harvesting to biological sensors depend on the modulation of LSPR. Through the synthesis and shape modifications of Au quasi-triangular nanoplatelets (QTP) arrays, LSPR modulation from near- to mid- infrared (~1.5µm to ~4.5µm) is revealed. Au QTP arrays are then associated to a thermochromic vanadium dioxide (VO_2) layer leading to a "smart" nanocomposite exhibiting modulated absorptions. The VO_2 layer acts as a phase change material with a tunable dielectric function vs. temperature and represents an active matrix. The dynamics of the geometric changes in QTP arrays and the phase transition of the matrix are directly correlated to the shift of the LSPR position ($\Delta\lambda_{LSPR}$~675nm). The experimental data are supported by a theoretical approach via the finite difference time domain (FDTD) method that provides the LSPR characteristics in the various Au QTP array and nanocomposite configurations. The experimental and modelling investigations prove that the red-shift resonance modulation originates from the creation of a temperature-dependent core-shell structure of Au QTP (core) surrounded by a thin metallic VO_2 layer (shell) and embedded into the VO_2 dielectric matrix.

1. Introduction

When atoms and molecules are exposed to electromagnetic fields, resonances will emerge in spectra as narrow peaks of absorption, emission, or scattering [1] and gives information's about the condensed matter. In the visible and infrared regions of the electromagnetic spectrum, the collective oscillations of free charge carriers in metallic systems such as nanoparticles give rise to some of the strongest resonances [2]. For micro/nanoparticles, the resonant frequency, i.e., surface plasmons resonance, is determined by the opto-geometric parameters corresponding to the metallic structure, such as nature (of the metal), size, shape, and the relative permittivity of the surrounding environment [2,3]. During a resonant light excitation, the free charge oscillations in the plasmonic structure can generate an intense electromagnetic field confined at the interface formed between a metallic system and its surrounding dielectric environment [3,4]. Such collective oscillations are called Localized Surface Plasmon Resonances (LSPR) [4]. Many applications have emerged from the field enhancement of the LSPR of specific optoelectronic devices, applications ranging from energy harvesting to ultra-sensitive physical, chemical, and biological sensors [5-7]. For all of these applications, developing adapted systems with a tunable LSPR position is a challenge of paramount importance [8-16]. Significant steps have been made, predominantly in the visible part of the electromagnetic spectrum through the geometrical manipulation of rounded noble metallic nanoparticles of Au and Ag elements associated to different surrounding environments [17-27]. Studies of the resonance modulation in the Near-/Mid- InfraRed (N/Mid IR) electromagnetic spectrum are more limited [28] despite the huge number of applications. In this range, organization at a micrometric scale of metallic micro-objects in a periodic way constitute a pathway for developing tunable LSPR platforms. Nature, size, shape, and shape dispersions of the objects constitute a key point to adjust the band of the LSPR [29,30]. A narrowband resonant mode could be more suitable for improving application performances [31,32].

Moreover, the choice of the surrounding dielectric environment (the matrix can be a gas, liquid, or thin films) is an additional option to jointly modify LSPR. When the metallic periodical arrays are integrated into conventional oxide matrices as Al_2O_3 [33] or SiO_2, the resonance position is modified but can no longer be adjusted. Integrating periodical micro-objects in a material with a variable permittivity will provide an interesting alternative to tune the LSPR.

In this article we propose to take benefit of the properties of a Phase Change/Transition Material (PC/TM), namely vanadium dioxide (VO_2) to tune LSPR. This oxide material well-known for its first order Semiconductor to Metal transition (SMT) close to room temperature (341K), presents drastic physical variations and consequently huge modifications in its optical properties [34]. These characteristics will be combined here with those of metallic periodic arrays. The study begins by evaluating the geometric changes undergone by an array of gold (Au) quasi-triangular nanoplatelets (QTP) during thermal treatment from room temperature (R_T) up to 1273K. The geometric changes are corroborated with an evolution of their plasmonic properties. The initial size of the Au QTP is tailored. The position of the LSPR peak is within the light transparent window of the Al_2O_3 substrate (200 nm up to 5 μm).

The preliminary step of monitoring the temperature induced geometric changes is essential to further develop an Au-QTP/VO_2 nanocomposite. Indeed, the synthesis of the VO_2 matrix by Pulsed Laser Deposition under reactive oxygen requires a deposition temperature at around 773K. This heating will probably affect the QTP shape and the original metallic sketch. Scanning electron microscopy (SEM) measurements is used to probe 'in situ' from R_T to 1273K the dynamics of QTP geometric changes versus temperature and examine phenomena of melting, nucleation, crystal growth and solid-state de-wetting. Moreover, High-Resolution X-Ray Diffraction (HR-XRD) furthers the study of the evolution of the crystallographic states. Major effects on the LSPR would be discussed.

Due to the variable dielectric function of VO_2 in the temperature range 293K - 363K, the developed Au-QTP/VO_2 nanocomposite could constitute an adaptable material with tunable peaks. To detail the properties of the nanocomposite architecture at the microscopic scale vs. temperature, particular attention is paid on their analyses using local Raman spectroscopy phase mapping in temperature. The experimental data are supported by a theoretical approach via the finite difference time domain (FDTD) method, which rigorously solves Maxwell's equations and allows to obtain the LSPR peak position in different configurations of QTP. Beyond their primary role of generating the LSPR, QTP are influenced by - or affect - the surrounding environment. So, the particles can be used as "live probes" to gather information about the surrounding material and probe for example the VO_2 transition. Following a sensing strategy, this new adaptive composite material can present the unique advantage to act as an optical transmitter in emission or absorption. Infra-red wavelength spectral absorption would be adjusted, modulated, and fixed at the maximum of sensitivity for the different used systems. For example, composites can be adapted for Surface-Enhanced Raman Spectroscopy (SERS) or rapid photo-detection applications.

2. Materials and Methods

Periodic arrays of particles on a supporting substrate can be grown by two different paths, *i.e.,* the so-called top-down or bottom-up methods [19,35,36]. An alternative methodology is provided by Nano-/micro-Sphere colloidal Lithography (NSL), which couples these two approaches. NSL takes advantage of the excellent control of geometric parameters offered by the top-down method and the excellent quality of particles given by the bottom-up approach. In the NSL procedure, a 2D colloidal crystal made from colloidal nano-/micro-spheres is used as a mask for subsequent material deposition [37]. Note that nano-/micro-spheres can be kept and used as a 2D colloidal crystal directly in the fabricated systems [38]. The arrays of particles are produced following the three steps presented in **Figure 1**. A monolayer of assembled monodisperse microspheres self-organizes spontaneously at the surface of a liquid to form a 2D hexagonal colloidal crystal. This structure is then transferred to a substrate (**Figure 1**a) by NSL, a procedure based on the Langmuir-Blodgett technique. In this resulting 2D hexagonal close-packed arrangement, the polystyrene microspheres cover an area on the substrate equal to $\pi/(2\sqrt{3}) = 90.7\%$, independent of their diameter. This geometric invariance makes possible to down- or up-size the geometry while keeping the same coverage. In this work, NSL experiments were performed using 3 μm diameter polystyrene microspheres (commercially available from *Microparticles GmbH* and *Micro Partikel Technologie GmbH*), deposited on *c*-oriented sapphire substrates, *i.e.,* Al_2O_3 (0001). Then 50nm of Au is deposited on/between the microspheres by Pulsed Laser Deposition (PLD) (**Figure 1**b and **Supplementary Material (A)**). The polymer microspheres used as a mask are then removed by dissolution with acetone (**Figure 1**c). The result is an array of Au quasi-triangular nanoplatelets (QTP) with a specific quasi-triangular based shape induced by a coupling of the colloidal mask shape given by NSL (initially seen by Fischer and Zingsheim [39]), and the high directional characteristics of the plasma plume (i.e., the flux of atoms) due to PLD deposition technique (see **Figure 1**).

The resulting specific ***a*** parameter (*i.e.,* the perpendicular bisector of the resulting quasi-triangular nanoplatelets, as presented in the insert of **Figure 2**a) of the QTP is related only to the ***D*** diameter of the polystyrene microspheres used for the fabrication of QTP arrays by the following equation [7]:

$$a = 3/2 \cdot \left(\sqrt{3} - 1 - 1/\sqrt{3}\right) \cdot D \qquad \text{Equation 1.}$$

For a 3 µm polystyrene microsphere, this relation gives a specific size ***a*** equal to 700nm, while the experimentally measured ***a*** parameter is approximatively 900nm. The difference can be explained by the presence of few defects in the packing of the polystyrene microspheres, their slight polydispersity, and the shading effects and migration of Au atoms below the polystyrene microspheres during the Au deposition process.

The deposition of Au metallic material was carried out in vacuum (10^{-8} mbar) and at room temperature, while the deposition of VO_2 was done in a reactive oxygen pressure of $2.2 \cdot 10^{-2}$ mbar and a temperature of 773K. PLD is implemented using a KrF excimer laser (TuiLaser AG, model "Thin Film Star" / TFS 100-248nm-CT-T V2.0) operating at a wavelength of 248nm, 25ns pulse duration, 10Hz repetition rate, and a fluence of 2-3J/cm^2. All the other equipments used in this study are listed and described in the **Supplementary Material (B)**.

The optical transmittance/absorbance of Au QTP arrays and Au QTP-VO_2 nanocomposites is measured by UV-VIS (0.8-3µm) and FTIR (1.5-5.5µm), using unpolarized light, and then modeled by a theoretical FDTD approach. The QTP arrays are simulated on an Al_2O_3-c substrate from real AFM images of the samples. The surrounding medium considered in the FDTD model is air (permittivity equal to 1) or VO_2. The simulated region presents periodic conditions in the *x* and *y* directions, and the array of QTP is considered infinite.

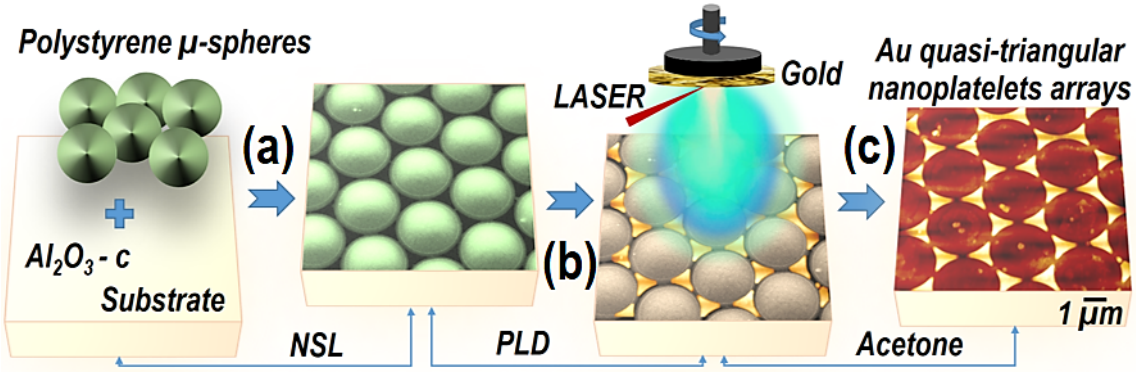

Figure 1. Schematic pathway for developing micro/nano-structured metallic architectures and consequently tunable LSPR platforms. a) Nano/micro sphere lithography, b) Pulsed laser deposition of Gold, c) Arrays obtained after removing the nano/micro sphere.

3. Results and discussions

3.1. Thermal treatments of Au QTP arrays

3.1.1. Geometric changes of the Au QTP arrays from 298K to 1273K

Gold is a noble metal with a very low affinity for oxygen, and its vapor pressure remains relatively low up to its melting point [40]. Au is non-miscible with vanadium, so there is no possibility of alloys. Thereby, it constitutes the ideal candidate for evaluating the QTP geometric changes as a function of temperature [41] and for the development of a vanadium based nanocomposite. Al_2O_3-c substrates are used due to their high chemical and thermal stability and their lack of reactivity with Au. Besides, these substrates are also very well suited for the growth of vanadium dioxide. The temperature at which the geometric characteristics of the particles are changed depends on various factors such as their size, their shape, the supporting substrate, etc. The nanometric dimensions lead to a decrease in the melting point of nanoparticles compared to melting temperature of Au bulk (~900K vs 1337K) [18,42]. Furthermore, pristine QTP shapes present a geometry close to a 2D thin object and consequently a huge number of surface atoms (compare to bulk atoms) which have a greater amplitude of vibration. Amongst all shapes, spheres have the lowest surface to volume ratio. This implies that QTP may melt at a lower temperature than their spherical counterparts [19,40,43-46]. At this scale, solid-state de-wetting mechanisms may also be present and drive the evolution of the shape of a particle to a more energetically favorable state [47,48]. The equilibrium morphology depends on the relative ratio between the three interfacial energies: particle-vapor (γ_{pv}), substrate-vapor or substrate surface energy (γ_{sv}), and particle-substrate interfacial energy (γ_{ps}). The expression of the thermodynamic equilibrium, given by Young equation, between the three phases is written as: $\gamma_{sv} = \gamma_{ps} + \gamma_{pv} \cos\theta$; where θ is the equilibrium contact angle at the three phases boundary [49]. The contact angle θ is calculated between 120° to 140°, close to 180°, proof of a total de-wetting process. Consequently, the system will minimize the total energy by driving each Au QTP towards a quasi-spherical Au nanoparticle. This is confirmed experimentally by the thermally driven shape evolution presented in **Figure 2**, from a low-temperature QTP toward a high temperature spherical shaped nanoparticle. **Figure 2**a-f shows the *in-situ* SEM evolution of Au QTP as a function of the thermal treatment temperature, starting from 298K (25°C) and up to 1273K (1000°C), with an average heating rate of 10K/min. At this point, the possible driving

mechanisms that can induce the surface energy minimization are solid-state de-wetting or/and melting. Other surface energy minimization mechanisms that can lead to the shape evolution of QTP, such as Ostwald ripening by evaporation or surface diffusion [50] and the coalescence phenomenon, are challenging to assess but cannot be ignored. However, based on Au's low vapor pressure and a relatively short thermal treatment duration, we can assume that QTP cannot lose or collect atoms and preserve their volume. This assumption is confirmed by different QTP and nanoparticles measurements at different temperatures using AFM (not shown here). A constant volume of ~$8 \cdot 10^{-3} \mu m^3$ is obtained. The geometrical evolution of Au QTP may be linked instead to the crystal growth induced by solid-state de-wetting.

From the SEM observation, it is possible to extract the step-by-step evolution of the Au QTP arrays towards Au nanoparticle arrays. During the thermal treatment process, different parameters are followed: the QTP projected area, the d_{tt} inter-QTP/nanoparticle distance, the substrate coverage ratio and the f shape factor defined as $4\pi A/P^2$where A is the QTP projected area, and P the perimeter (for theoretical QTP, $f = 0.21$, for spherical nanoparticles, $f = 1$ (see insert **Figure 2**i)). All these markers show the presence of three temperature range regimes: 298K to 723K, 723K to 823K, and 823K to 1273K. For example, following the shape factor, the first regime implies small f modifications from 0.66 to 0.71. In the second regime, over a small temperature range (100K), the thermal treatment has a significant impact, f evolves from 0.71 to 0.84. Above 823K, the temperature effect on the geometric characteristics is less noticeable, f varies from 0.84 to 0.90 over more than 450K. Remarkably, most of the Au QTPs shape evolution is produced within a temperature interval of 100K, between 723K and 823K, after which the QTP arrays can be considered as a nanoparticle array.

A particular situation, pointed out in **Figure 2**h, presents two configurations, e.g., individual QTP vs connected QTP. As the temperature rises above 723K, the connected QTP split into two individual ones, additionally proving the QTP are not subjected to the coalescence effects.

Finally, the thermal treatment has a triple effect; it changes the QTP geometry, improves the QTP/nanoparticle array quality, and provides a way to slightly modulate the optical transmission amplitude (area coverage from 9.3% (at 298K) to only 3.5% (at 1273K)). Note that the effect of a conventional furnace produces the same geometric metallic sketch versus temperature (**Supplementary material (A**).

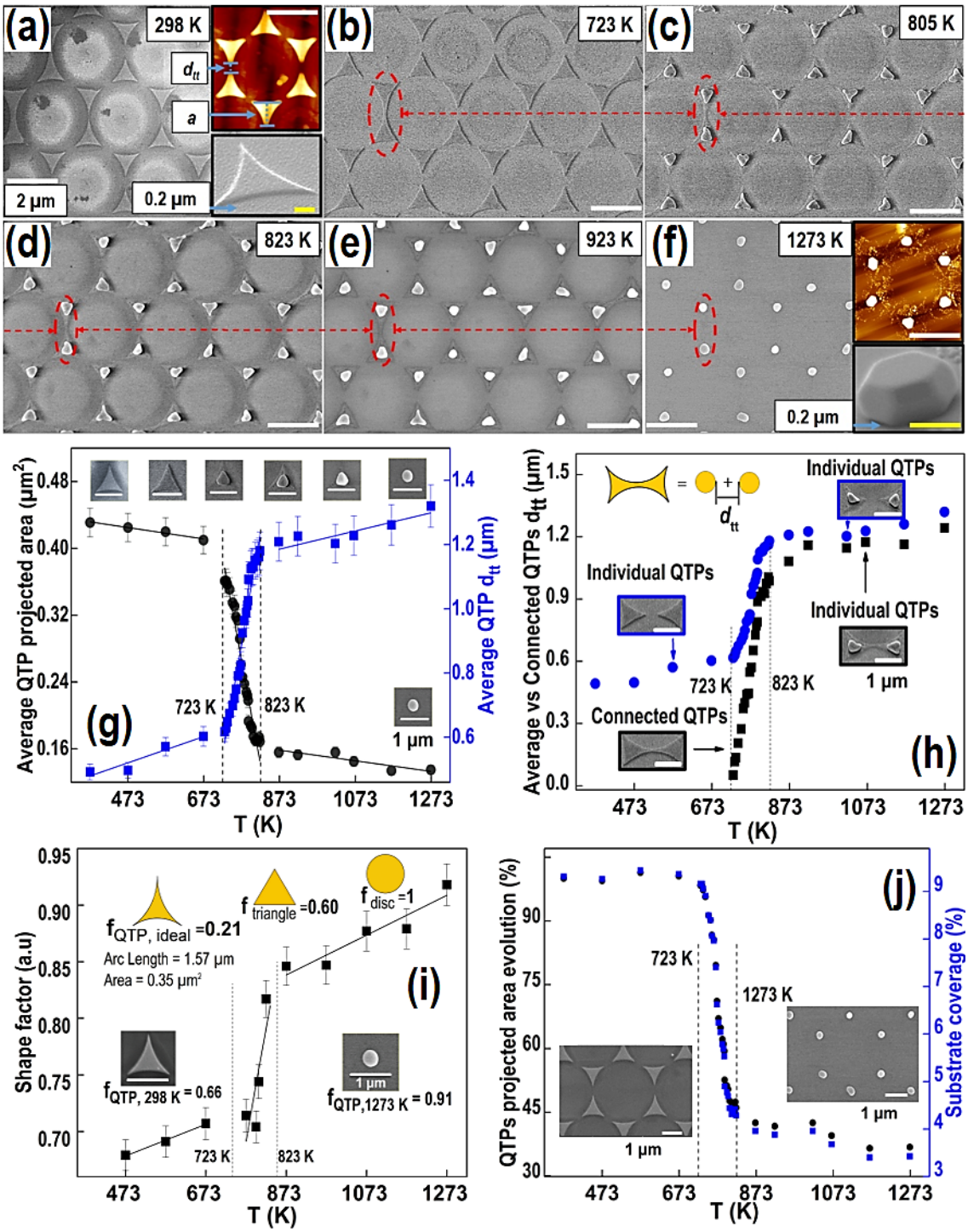

Figure 2. Thermal treatments of Au QTP arrays. a-f) Thermal treatments imaging by *in-situ* SEM. The inserted images in a) and f) are made by AFM and SEM. The white scale bar (resp. yellow) is equal to 2µm (resp. 0.2µm). g) Effects of thermal treatment on the QTP projected area and inter- QTP distance (tip-to-tip) d_{tt}. h) Evolution of inter- QTP average distance between the tips of non-connected/connected adjacent QTP before/after the thermal treatment. i) Shape factor of QTPs as a function of the thermal treatment temperature. j) QTP projected area and substrate coverage as a function of temperature. The data from g)-j) are extracted from the step by step *in-situ* SEM observation.

3.1.2. Crystallographic evolution of the Au QTP arrays from 298K to 1273K

To understand deeper the solid-state de-wetting process and the perfect atomic organization (Winterbottom construction [51,52]), θ-2θ X-ray patterns are performed at room temperature. It reveals that the Au QTP are crystalline and mono-oriented, having just a 111 reflection. However, this measurement is not sufficient to completely characterize the QTP. We therefore recorded XRD reciprocal space maps (RSMs) around the 111 reflection of Au in a 298K – 1273K temperature range.

Figure 3a-d shows the evolution of the 2D diffracted intensity around the 111 reflection of Au as a function of the thermal treatment temperature (heating and cooling). In **Figure 3**a the reflection located at Q_z = 2.66 (red/black region) corresponds to the 111 reflection of Au, while the maximum centered around 2.63 (green region) comes from the 111 reflection of the tantalum holder used to secure the sample during the high-temperature measurement. At 298K the 111 reflection of Au exhibits a significant spreading and curvature perpendicular to the [111] surface normal. As *θ-2θ* XRD characterizations, it indicates that, although a (111) preferred orientation exists. This orientation is far from perfect crystal and significant mosaicity is observed (**Supplementary material (C)**), a classical result obtained for fcc metallic PLD deposition at room temperature. With the annealing process, two distinct phenomena are observed. The 111 reflection shifts towards lower values (i.e., higher lattice spacings) because of thermal expansion. While cooling back to the initial state at R_T, the reflection recovers its initial position. Furthermore, the diffracted intensity significantly coalesces in the central region of the map (i.e., $Q_x = 0$) and forms a well-defined peak. The crystalline orientation of the QTP improves and reaches a single crystal-like quality. This is further attested by the formation of "streak" parallel to the Q_z direction, consecutive to the formation of surface facets at high temperatures.

In addition to the well-defined Bragg reflection, an elongated low intensity remains, proof of the presence of small misoriented crystallites. All these features are also clearly visible in the rocking-curve (RC) (**Supplementary material (C)**).

The existence of a critical temperature range, between 723K to 823K, where the significant Au QTP geometrical evolution occurs, coupled with the facet forming phenomenon seen at 823K (**Figure 2**f, **3**b), tends to underline temperature as the main parameter to induce the following solid-state de-wetting scenario.

In the early stages of the solid-state de-wetting, the morphology of Au QTP change via surface self-diffusion of Au atoms (up to 723K). Then, the thermal energy reaches a sufficiently high value so that the crystallites with low interfacial energy start to consume the ones that have higher interfacial energy, which results in the facet forming phenomenon observed at 823K. These facets will later evolve with temperature but do not strongly affect the morphology, as they do between 723K and 823K.

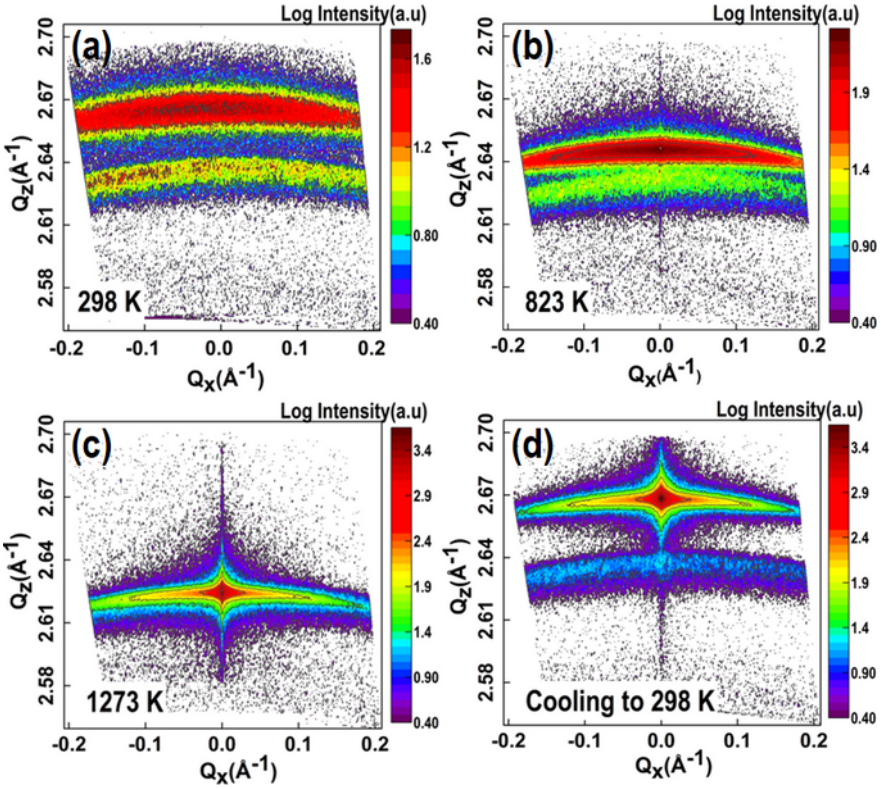

Figure 3. a-d): *in-situ* HR-XRD scan; Reciprocal space mapping of the 111 Au QTP reflection as a function of the thermal treatment temperature, heating/cooling cycle from 298K up to 1273K. The maps are plotted as a function of the diffraction space coordinates Q_z and Q_x, respectively corresponding to the out-of-plane and in-plane component of the scattering vector $Q = 4\pi * \sin\theta / \lambda$.

3.1.3. LSPR measurements and calculations of the thermally treated Au QTP arrays.

Absorbance is calculated and compared directly with the experimental measurements (see **Figure 4**a-b). In the model, the single cell composed by 6 QTP interacts with a circularly polarized light to get as close as possible the experimental conditions (unpolarized light). During a measurement, several monodomains (>200), differently oriented, are illuminated. The experimental response of optical absorption results from an average over a set of randomly oriented mono-domains. It seems strongly probable that linear polarization effects of light could be present but, in that paper, the conditions are not met. The values of optical indices for Au were fitted in the spectral range extending from 0.8µm up to 5.5µm [53].

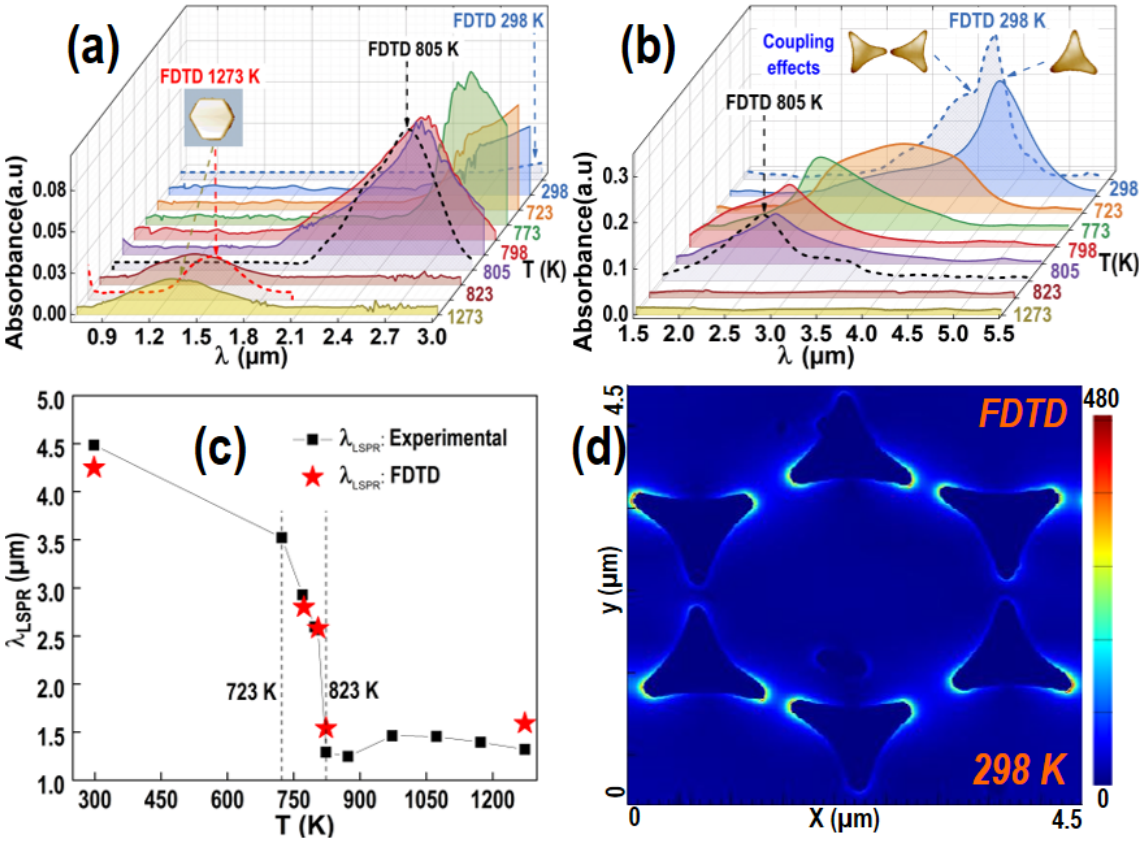

Figure 4. Localized Surface Plasmon Resonance (LSPR) of Gold Quasi-Triangular nano-Platelets (QTP) arrays. Absorbance measurements as a function of temperature: a) by UV-VIS and b) by FTIR. Continuous lines (resp. dotted lines) represent experimental measurements (resp. FDTD calculation). c) Comparison of the experimental and theoretical LSPR peak positions. The peaks are extracted from a fit with a Voigt function of the experimental absorbance spectra for each temperature from a)-b). d) Electric field cartography at $\lambda = 4.45\ \mu m$ corresponding to the Au QTP before thermal treatment. The Electric field cartography of the coupling effects between QTP and the Electric field cartography of QTP treated at (805K, 823K and 1273K) is reported in the **Supplementary Material (D).**

Before thermal treatment, the Au QTP arrays has a strong resonance in the absorbance spectrum with a maximum located at $\lambda_{LSPR} \approx 4.45\ \mu m$ (see **Figure 4**b). The FDTD approach (**Figure 4**d) points out that for $\lambda_{LSPR} \approx 4.25\ \mu m$ the polarized electric field enhancements are located on QTP corners and correspond to the dipolar localized surface plasmon resonances (LSPR). The model and the experimental measurements are in good agreement, the slight differences can be attributed to Au's theoretical optical indices used in the simulation and the non-perfect compliance of the QTP on large area. Note that experimental measurements are made on 20mm^2, calculations on only limited area of 20µm^2.

At 298K, the smaller gap between QTP leads to plasmonic coupling effects highlighted by the intensity of the electric field distribution between the adjacent QTP that following the dipolar resonance (**Supplementary**

Material (D)). Coupling effects appear in the calculated optical absorbance spectrum of the sample at 298K as a shoulder ($\lambda_{LSPR} \approx 3.7\,\mu m$) (**Figure 4**b, blue dotted line). As the heating process increases, the resonance starts to blueshift in wavelength position (**Figure 4**a-b). After 823K, the resulting Au nanoparticle arrays have a resonance in the absorbance spectrum with a maximum located at $\lambda_{LSPR} \approx 1.45\,\mu m$. This peak position remains unchanged by further thermal treatments up to 1273K.

On Figure 4c, a sump-up of the comparison between the modeled and measured LSPR positions show good agreement. Small differences can be explained by the theoretical optical indices introduced in the model and the Au QTP size distribution [54].

At 805K, also appears an absorption peak in the visible part of the optical spectrum ($\lambda_{LSPR} \approx 0.50\,\mu m$¿ which is present in all the samples thermally treated beyond 805K. This LSPR (confirmed by FDTD) originates from the Au atomic residue left behind after the removal of the original polystyrene microspheres (**Supplementary Material (D)**). Indeed, upon thermal treatment, melting and coalescence effects occur and Au nanoparticles are formed with a diameter close to 10nm, giving the signal observed in the visible regime. As there is no physical interaction between the residual nanoparticles and the Au QTP (**Supplementary Material (D)**), these residual nanoparticles, involuntarily initially present, act as witness particles to justify the absence of the Ostwald ripening phenomenon.

3.2. LSPR modulation through adaptive metal-ceramic periodic arrays; Au-QTP/VO_2 nanocomposite formation.

3.2.1. Microstructural, structural, optical and STM characteristics of nanocomposites

A metallic-ceramic composite is fabricated by covering the Au-QTP by a VO_2 matrix. Inside this composite, as usual, interactions between the metallic QTP and the VO_2 layer can affected/degraded the behavior of each of entity. The microstructure, controlled by SEM and AFM of the VO_2 layer of the nanocomposite remains almost unchanged compared to a conventional thin film of VO_2 (not shown here). For the metallic inclusions, VO_2 layer acts as a 'blanket' (**Supplementary Material (E)**). As expected, and demonstrated in the first part of the paper, the morphology of the Au-QTP is mostly influenced by the temperature deposition of VO_2. At 773K, the metallic inclusion shapes start to be modified but the global triangular shape remains (**Supplementary material (E)**). EDS investigation (Energy Dispersive X-Ray Spectroscopy) provides complementary information about the spatial distribution of the different elements (V, O, Au). On one unit cell 6×6 μm^2, the three elements are distributed in accordance with the initial structure of the composite (**Supplementary Material (E)**). Diffusion processes during composite synthesis are probably weak. Chemical etching performed on the composite removes the VO_2 layer and reveals thermally affected Au-QTP but still recognizable. In addition to the microstructure, atomic structure and optical properties are of paramount importance to ensure the presence of a nanocomposites with preserved excellent SMT characteristics (**Supplementary Material (E)**). We compared the atomic structure and transmittance of a VO_2 thin film and the Au-QTP/VO_2 nanocomposite of both 200nm in thickness ~~are investigated~~. **Figure 5**a reports the thermal hysteresis of the optical transmittance at a wavelength of 3μm of thin films of VO_2 with or without Au QTP. As a positive point, the two samples, deposited in the same conditions, have practically the same thermal hysteresis behavior and width (~ 4K (insert **Figure 5**a)). The difference in the SMT temperature (**Figure 5** a), 345K vs. 347K, for VO_2 thin film with or without QTP respectively, can be explained by the presence of the metallic inclusions, which may induce various physical phenomena like the electron injection from the metal to the oxide (electronic work function Au (4.8eV) vs. $VO_{2monoclinic}$ (5.4eV)), the creation of oxygen vacancies, the symmetry breaking at the Au/VO_2 interface and, most likely, the strain/stress development between QTP and VO_2. All these phenomena are briefly discussed in the **Supplementary Material (F)**. The optical transmission contrast (**Figure 5a**) is approximately 7% lower for the sample containing Au QTP. The value of 7%, not so far from the 9% expected (see also **Figure 2**j), is a consequence of the beginning of solid-state de-wetting and the associated Au QTP shape modifications during VO_2 deposition.

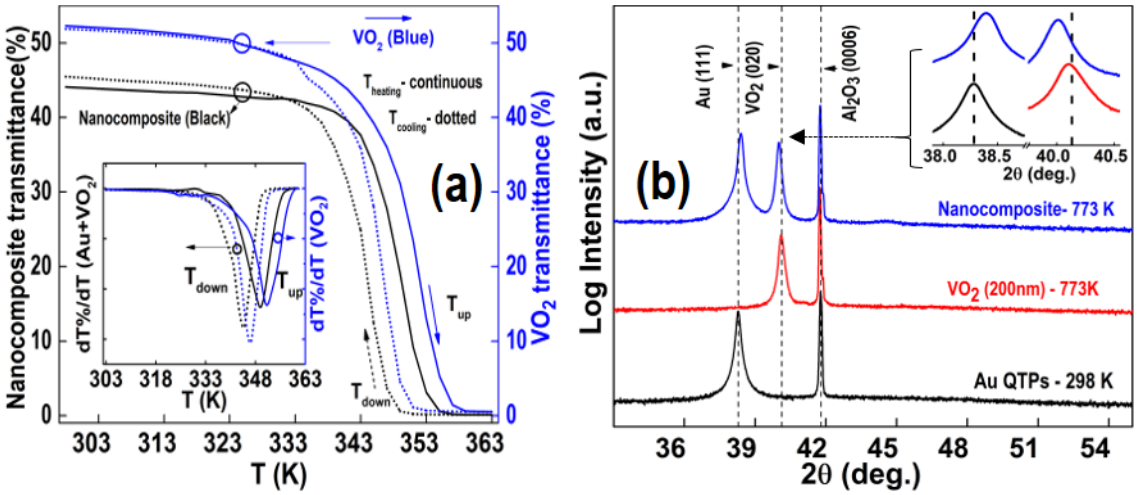

Figure 5: a) Temperature dependence of the optical transmittance at 3 μm of the 200nm-nanocomposite (Au-QTP/VO_2) vs. 200nm-VO_2 thin film. b) XRD patterns of Au QTP, VO_2 thin film, and nanocomposite.

Figure 5b shows the X-ray patterns recorded at room temperature of pristine Au QTPs and VO_2 thin film with or without Au QTP. As discussed earlier, the presence of the (111) orientation from Au reveals that the Au QTP are crystalline and mono-oriented, with a face-centered cubic (fcc) structure. Embedding QTP inside VO_2 does not change the XRD diagrams. In both cases, VO_2 is mono-orientated, having a monoclinic structure with a (020) orientation (**Figure 5**b).

Table 1. Crystallographic characteristics of the Au QTP, VO_2 thin film and the Au-QTP/VO_2 nanocomposite

Sample	$Au(111)_{FCC}$ peak		$VO_2(020)_M$ peak		Strain (%)	
	Position (2θ)	FWHM (°)	Position (2θ)	FWHM (°)	e_{Au}	e_{VO_2}
Au QTP	38.17	0.13	-		0	-
VO_2	-		40.04	0.15	-	-0.354(5)
Au QTP + VO_2	38.31	0.14	39.93	0.13	-0.270(1)	-0.284(2)

The peak position and FWHM of all the samples are extracted using a Voigt fit of the XRD data

In both samples, VO_2 is epitaxial with the usual orientation corresponding to the Al_2O_3-c substrate: $(010)_{VO_2} \parallel (001)_{Al_2O_3}$; $[100]_{VO_2} \parallel [210]_{Al_2O_3}$, $[100]_{VO_2} \parallel [-110]_{Al_2O_3}$ and $[100]_{VO_2} \parallel [120]_{Al_2O_3}$. Au QTP are not epitaxial with a (111) preferred orientation (with rocking curve width of roughly ~8.7°). The pristine Au QTP are strain-free on the Al_2O_3-c substrate. The 200nm VO_2 thin film is compressively strained in the out-of-plane (oop) direction because of the thermal expansion mismatch with the Al_2O_3-c substrate [55]. In the nanocomposite Au QTP-VO_2, the VO_2 matrix exerts compressive strain on the QTP in the oop direction. The effect of strain is visible in the θ-2θ scan, where the Au (111) peak is shifted towards larger angles (**Figure 5**b). The diffraction peak position of (020) VO_2 in both cases differs from the theoretical value of 2θ = 39.76°, because of the above-mentioned strain (see **Table 1** and **Figure 5**b). The decrease of the compressive strain, in the case of Au QTP-VO_2 thin film is consistent with a decrease in the SMT temperature compared to the SMT of VO_2 thin film alone [60]. In VO_2, the strain alters the orbital occupancy near the Fermi energy level E_F. The higher compressive strain along the oop direction of the VO_2 thin film alone makes the d_{II} and π* orbitals shift upward and the d^*_{II} orbital downward in rapport to the Au QTP-VO_2 sample [56]. Consequently, the higher oop compressive strain along the b_M direction in the 200 nm VO_2 thin film alone increases the size of the insulator state's band gap, leading to a higher energy barrier and a higher SMT temperature. Strain/stress probably plays an essential role [56] in these samples.

3.2.2. Optical properties of the Au-QTP/VO_2 nanocomposite

Figure 6 shows the experimental and calculated absorbance spectra of the Au-QTP/VO_2 nanocomposite array, the temperature dependence of its resonance, and the results of the simulated *E*-field distributions upon light interaction. On **Figure 6**a (top panel), two resonance peaks ($Peak_I$ and $Peak_{II}$) arising from nanocomposites (100nmVO_2/Au-QTP) are clearly visible.

The double plasmonic peaks (compare to the previous single LSPR) may be linked to a selective E-field enhancement at different interfaces [57]. Considering the discussed nanocomposite, the presence of VO_2 obviously increases the number of interfaces (Au QTP-substrate, Au QTP-VO_2, substrate-VO_2) and may also explain the small difference in intensity between the two peaks. As a proof, the etching of the VO_2 layer makes it possible to obtain the original single peak (not shown here).

At R_T, experimental $Peak_I$ and $Peak_{II}$ are located respectively at $4.78\,\mu m$ and $3.52\,\mu m$. A FDTD model is developed by starting from the AFM experimental image of the Au QTP revealed by chemically post-etching the VO_2 matrix. The FDTD model (*FDTD-N_I*) of the absorbance spectra confirms the two peaks close to the measured values ($Peak_I$, resp. $Peak_{II}$ located at $4.15\,\mu m$, resp. $3.55\,\mu m$¿ (**Figure 6**a bottom panel). The difference between the experimental and calculated data are induced by the thickness of the VO_2 which must be limited to 50nm in the model (At 100nm, the metallic VO_2 matrix shunt entirely the signal) and by the incomplete reproducibility of the QTP geometry on large area. Nevertheless, the E-field distributions extracted for both peaks suggest plasmonic nature with dipolar characteristics (**Figure 6**c-d).

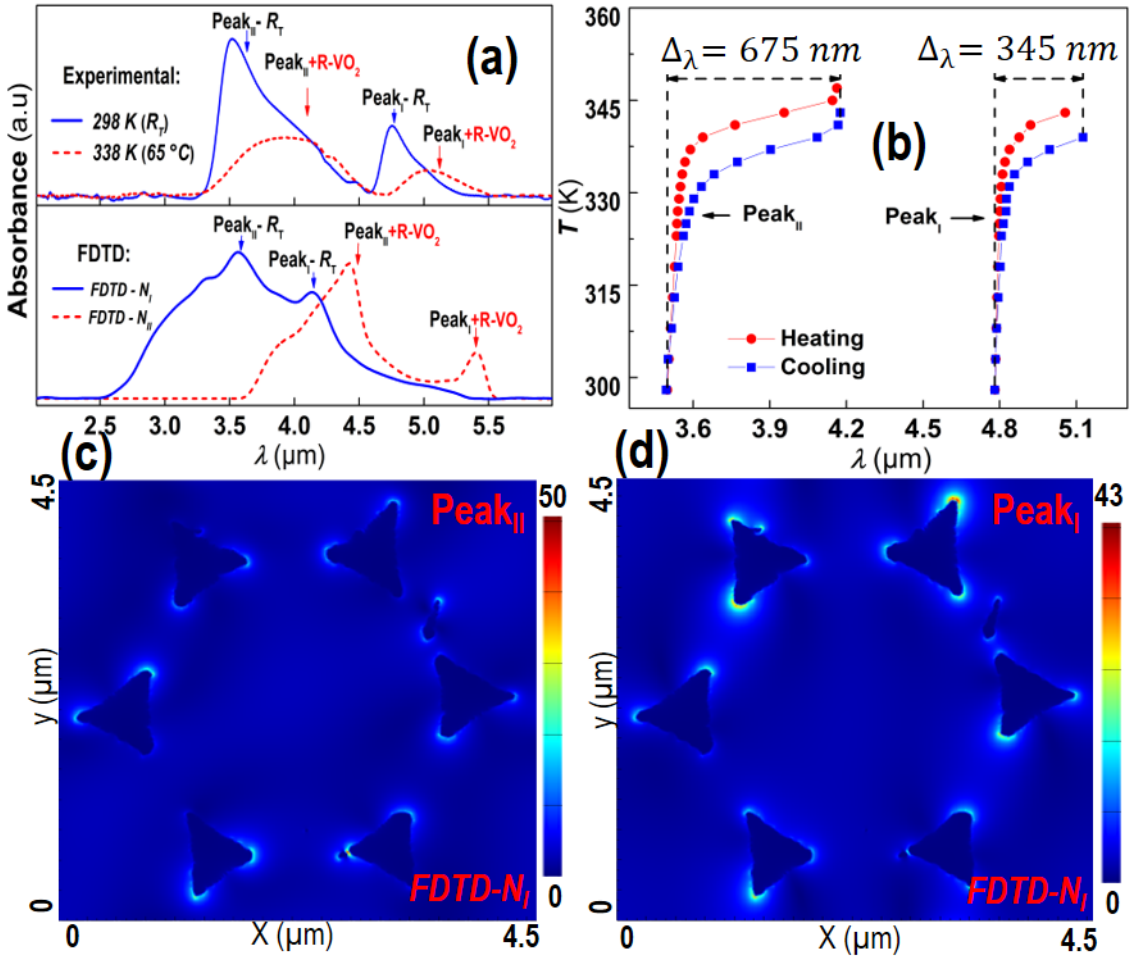

Figure 6: Localized Surface Plasmon Resonance (LSPR) of Au-QTP/VO_2 nanocomposite. a) Absorbance spectra of nanocomposite at two temperatures (298K and 338K), experimental (top panel) vs theoretical (bottom panel) curves. b) Temperature dependence of the LSPR position measured during a heating/cooling cycle. c-d) Electric field cartography (Finite Difference Time Domain (FDTD)) for the two resonant peaks at: $\lambda = 4.15\,\mu m$ ($Peak_I$) and $\lambda = 3.55\,\mu m$ ($Peak_{II}$) (model *FDTD-N_I*). The Electric field cartography corresponding to *FDTD-N_{II}* is reported in the **Supplementary material (D) - Figure S6**.

At higher temperature (338K) (**Figure 6**a, top panel), both peaks are red shifted compared to their R_T counterparts. **Figure 6**b shows the step-by-step evolution of the LSPR position during heating and cooling which correspond to the VO_2 matrix hysteresis behavior. Experimentally, the maximum modulation amplitude for $Peak_{I \text{ and } II}$ are respectively $\Delta\lambda$=345nm and $\Delta\lambda$=675nm (**Figure 6**b), remarkable large range, largest than the visible spectrum (~400nm).

This strong active LSPR modulation can be induced by a change in the dielectric characteristics of VO_2 during SMT [58] or/and by a VO_2-QTP coupling phenomenon. There are two possible types of QTP coupling that affect the LSPR peaks position through the near-field and far-field interactions [59]. On one hand, the far-field interaction at the long-range produces a red shift of the LSPR peaks as the distance between QTP increases. On the other hand, near-field interaction at short-range results in a blue shift of the LSPR peaks as the distance between QTP increases. Inside the nanocomposite discussed in this paper, the distance between QTP remains stable and constant and does not affect the coupling. Therefore, the red shift of LSPR peaks originate from the VO_2 component of the nanocomposite. A possible origin of the active wavelength red shift in LSPR peaks during SMT can be induced by the VO_2 transition at specific zones inside the nanocomposite. During heating, a thin shell of metallic VO_2 may be formed around the Au QTP while the rest of the VO_2 remains in the semiconductor-like state. This VO_2 metallic shell can "artificially" increase the size of the "metallic QTP zone", leading to a red shift of the LSPR peaks (due to long-range plasmon coupling) based on the far-field interaction. And effectively, an increase of the metallic QTP size results in the red shift of the LSPR [60]. This is possible since, in the metallic VO_2, the Fermi level is located in the t2g(π* orbital) level, which is partially overlapped with the t2g(d//orbital) level. In this configuration, the optical excitations of metallic VO_2 are governed by three interband transitions E_1, E_2, and E_3 occuring at around $\sim$1.22eV, $\sim$3.37eV, and $\sim$5.90eV, respectively [61]. The strain alters the orbital occupancy near the Fermi energy level, and since the E_1 transition corresponds to the optical excitation from the filled t2g(d//) to the empty t2g(π*) bands, this transition broadly exists in the range 0.5–2eV [62]. Hence, the metallic VO_2 can also support plasmon resonances based on free carriers intraband excitations in the conduction band. This strengthens the hypothesis of a shell of metallic VO_2 increasing the size of the QTP can be the origin of the LSPR red shift through far-field interactions during SMT.

A second FDTD model (*FDTD-N_{II}*) is developed to support the hypothesis of resonance peaks red shift and the metallic core-shell structure (**Figure 6**a bottom panel). *FDTD-N_{II}* consists of Au QTP (core) enveloped by metallic VO_2 (shell) and embedded in 50nm of a semiconducting VO_2 matrix. The size of the metallic VO_2 shell is taken $\sim$10% larger (on the x-y directions) than the size of the Au QTP. For confirmation, the size of the pristine Au QTP was post-revealed experimentally by chemically removing the nanocomposite VO_2 component. As for the first model, the *FDTD-N_{II}* model points out the presence of two resonance peaks. Both peaks being red shifted from their *FDTD-N_I* equivalents ($Peak_I$ 4.15µm$\rightarrow 5.42\,\mu m$ and $Peak_{II}$ 3.55µm$\rightarrow$4.40µm). The *E*-field distributions extracted from *FDTD-N_{II}* model show that the plasmonic dipolar characteristics of both peaks are maintained after the introduction of the metallic VO_2 shell (**Supplementary Material (G)**). The FDTD approaches (*FDTD-N_I* and *FDTD-N_{II}*) show qualitatively that the nanocomposite Au QTP-VO_2 resonances have a plasmonic origin and the red shift during SMT is induced by the formation of an adaptive core-shell structure. The FDTD calculations are made on a limited area (4.5×4.5) µm^2 for *FDTD-N_I* and (1.5×1.5) µm^2 *FDTD-N_{II}*) far smaller than the one used in experimental measurements ($\approx$20 mm^2), explaining differences between the calculated and the experimental results. Moreover, some experimental details of the QTP that cannot be exactly captured by the FDTD models, cannot be considered. The experimental absorbance spectra must be thought as the envelop function of the response of multiple regions on which FDTD calculations are made.

3.2.3. Experimental investigation of the formation of core-shell structure within the nanocomposite.

To identify structural changes that can support the LSPR peaks red shift during SMT (**Figure 7**), temperature-dependent Raman point measurements are performed on the nanocomposite.

In the VO_2 material, the Raman peaks are attributed to V-V (ω_1 and ω_2) and to V-O (ω_o) vibrational modes [63]. Semiconductor VO_2 has the monoclinic M1 and M2 and triclinic T phases [64,65]. The M2 phase is distinguished from the M1 phase mainly by the red shift of the ω_o frequency, whereas T demonstrates similar spectral features to the monoclinic ones [57,63]. The vibrations are assigned as follows: at 575cm^{-1} to T phase, 614cm^{-1} to M1 phase, and 640cm^{-1} for M2 phase [63-67]. Special attention is paid to the V─O vibrations to identify the VO_2 phases in the nanocomposite. A fit of the Raman bands using a mix of Lorentz and Gaussian functions is used to identify and assign the Raman modes to the corresponding VO_2 phases. The temperature-dependent Raman signatures of VO_2 of two distinct positions (**Figure 7**a) on the nanocomposite are displayed in **Figure 7**b. The I- and II- zones correspond respectively to the top (close to) of Au QTP and zones free of metallic structures. To simplify, I-zone is associated to the core of the metallic QTP, II-zone is related to the matrix. As the temperature increases from R_T to 350K, the signatures of M1, M2, and T disappear, giving way to an absence of peak, proof of the rutile, R phase (**Figure 7**b).

The semiconductor VO_2 in I-zone transforms into the R phase at a lower temperature compared to the II-zone, in good agreement with the core-shell structure suggested by previous investigations. To visualize the spatial 2D (x-y) distribution of the VO_2 phases and the core-shell structure, Raman spectroscopy mapping is performed (**Supplementary Material (H)**) on an area of approximatively 5×5 µm^2, as a function of temperature

from R_T to 350K. The reconstructed Raman maps shown in **Figure 7**c give a spatial repartition of the phases M1, M2 and T. A_g mode at 575cm^{-1} of T is less intense than A_g of M1 and M2 [63,68].

At R_T, VO_2 semiconductor phases, M1, M2 and T are spatially distributed everywhere. The intensity of the M1 is noticeably higher in the I-zone compared to the II-zone (**Figure 7**c). The opposite distribution is observed for the M2 phase. Spatial distribution of the T phase is homogeneous. As the temperature rises (338K), the M2 zone slightly increases (a part of VO_2 transited from M1 to M2 phase). As the temperature rises more ($\geq$343K), the presence of the Rutile phase is identified through the lack of Raman response (metal characteristic). This transition is a gradual process. All the semiconductor phases (M1, M2, T) start to disappear first at the region corresponding to QTP ((**Figure 7**c, regions materialized by circles). Finally, when corroborating the intensities of the M1, M2 and T phases with spatial repartition, the co-existence of VO_2 semi-conductor and metallic structure within VO_2 material is confirmed.

At a temperature closed to the SMT, the nanocomposite is composed by Gold QTP surrounded by VO_2 thin metallic layers inside a VO_2 semi-conductor matrix. This specific structure confirms the red shift LSPR previously observed.

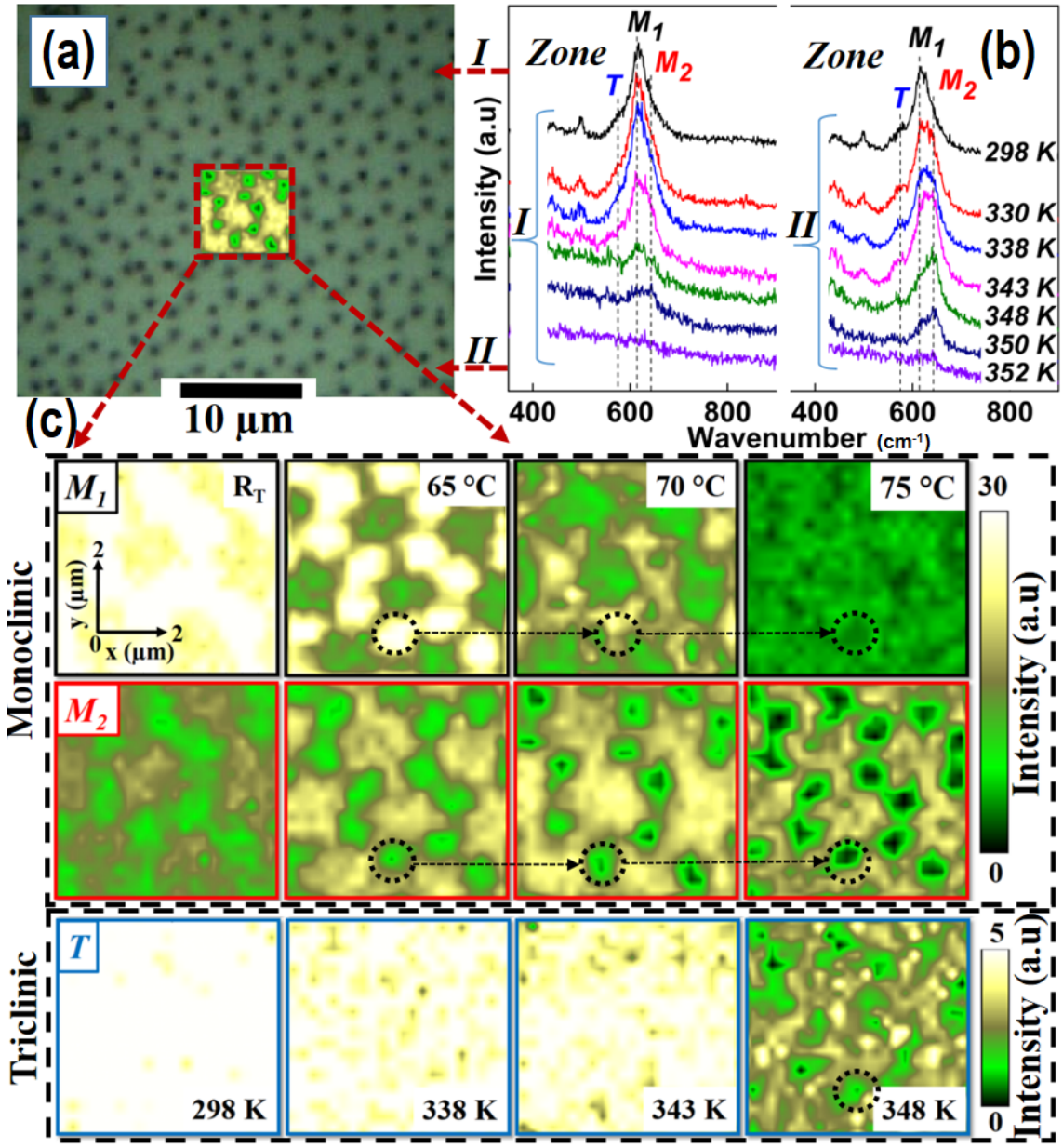

Figure 7. Raman spectroscopy measurements of Au-QTP/VO_2 nanocomposite. a) Optical image of the nanocomposite used for the measurements. b) Temperature-dependent Raman point measurements of the nanocomposite (zone I → top and close to the QTP and zone II → space between QTP). c) Nanocomposite Reconstructed Raman maps showing by color contrasts the variation of the intensities of each fitted mode (M1, M2 and T). The reconstructed maps give a spatial repartition of the M1, M2 and T phase in relation to the QTP position during a heating cycle.

4. Conclusion

The association of Langmuir-Blodgett and Pulsed laser deposition processes is presented and allows to develop specific nanocomposites formed by micro-quasi-triangular nanoplatelets (QTP) arrays embedded in VO_2 matrix thin films.

Due to the fabrication temperature imposed for VO_2 synthesis (~773K), a necessarily and initial study on the QTP behavior versus temperature is first carried on. This investigation shows that the thermal treatment promotes shape and structure modifications of the metallic sketches. A specific temperature range (723K-823K) is identified where the major's transformations occur. The Au QTP evolve under a solid-state de-wetting process on Al_2O_3-c substrates. The developed arrays exhibit strong Localized Surface Plasmon Resonance (LSPR) in the Near and Mid InfraRed regime (N/Mid- IR) between ~1.5µm to ~4.5µm adjustable with the continuous modifications of the QTP shape. These experimental results are corroborated by a theoretical Finite-Difference Time-Domain approach (FDTD). Moreover, during the heating process, the Au QTP evolve from systems with a weak crystallographic orientation to perfect crystals through thermal treatment.

As expected, the synthesis of a nanocomposite based on Au-QTP/VO_2 allows the modulation of the LSPR amplitude and wavelength versus temperature in the N/Mid-IR regime, while keeping the optical properties of the VO_2 phase-change material matrix.

During the SMT transition of the VO_2 matrix, between 298K and 338K, the LSPR shift is at around $\Delta\lambda$=675nm. Based on rigorous investigations by FDTD modelling, spectroscopy and local Raman measurements, the origins of this red shift are identified. The nanocomposite resonances have a plasmonic base and the red shift during SMT transition of the matrix is explained by the formation of an adaptive core-shell metallic structure. The core is composed by the gold metal of the QTP, the shell by a thin metallic VO_2(R-phase) layer starting at their interface, the whole embedded into a VO_2(M1-phase, M2-phase, T-phase) semiconducting matrix. Indeed, as the temperature rises, a VO_2(R-phase) shell starts to grow on and close to the Au QTP surface, while the rest of VO_2 follows normal transition pathways. This R-phase shell "increases the total volume" of the metallic QTP and induces the red shift of the wavelength position of the LSPR peaks.

The formation of the VO_2 metallic shell causes the Au-QTP/VO_2 nanocomposite to behave like an adaptive periodic metal architecture. This new approach may be further adapted in other Mott-type insulating oxide systems towards implementing Mott-type practical applications for electronic and optics devices.
Moreover, QTP /VO_2 based system appears as ideal candidates readily tunable to specification to enhance the IR modes of specific chemical moieties/compounds for more straightforward sensing and detection. This nanocomposite should be helpful for the sustainable development of applications based on surface-enhanced infrared absorption spectroscopy, for analyzing of exceptionally low quantities of molecules.

Funding and acknowledgements:
This work was partially supported by the LabEx ∑-lim ANR-10-LBX-0074-01 (50% of Dr. Adrian BERCEA's PhD thesis), laboratory of excellence launched by the French Ministery of Higher Education and Research (https://www.unilim.fr/labex-sigma-lim) between the XLIM (https://www.xlim.fr) and IRCER (https://www.ircer.fr) Research Institutes.
This work also benefited from financial support from the ANR-16-CE24-0025 and technical support from CARMALIM platform regrouping instruments and investigation techniques of the University of Limoges.

Author Contributions: Conceptualization, Adrian Bercea, Frédéric Dumas-Bouchiat, Catalin Constantinescu, Corinne Champeaux; Formal analysis, Adrian Bercea, Frédéric Dumas-Bouchiat, Alexandre Boulle, Julie Cornette, Maggy Colas, Sylvain Vedraine, Corinne Champeaux, Catalin Constantinescu ; Writing - original draft, Adrian Bercea, Frédéric Dumas-Bouchiat; Writing - review & editing, Adrian Bercea, Frédéric Dumas-Bouchiat; Supervision, Frédéric Dumas-Bouchiat, Corinne Champeaux, Catalin Constantinescu; All authors have read and agreed to the published version of the manuscript.

Conflicts of Interest: The authors declare no conflict of interest

References

[1] M.I. Stockman, Dark-hot resonances, Nature. 467 (2010) 541–542.
https://doi.org/10.1038/467541a.
[2] F. Papoff, B. Hourahine, Geometrical Mie theory for resonances in nanoparticles of any shape, Opt. Express. 19 (2011) 21432–21444.
https://doi.org/10.1364/OE.19.021432.
[3] S. Vedraine, R. Hou, P.R. Norton, F. Lagugné-Labarthet, On the absorption and electromagnetic field spectral shifts in plasmonic nanotriangle arrays, Opt. Express. 22 (2014) 13308–13313.
https://doi.org/10.1364/OE.22.013308.
[4] Z. Zhang, X. Jiang, B. Liu, L. Guo, N. Lu, L. Wang, J. Huang, K. Liu, B. Dong, IR-Driven Ultrafast Transfer of Plasmonic Hot Electrons in Nonmetallic Branched Heterostructures for Enhanced H2 Generation, Adv. Mater. 30 (2018) 1705221.
https://doi.org/10.1002/adma.201705221.
[5] X.-C. Ma, Y. Dai, L. Yu, B.-B. Huang, Energy transfer in plasmonic photocatalytic composites, Light Sci. Appl. 5 (2016) e16017.
https://doi.org/10.1038/lsa.2016.17.
[6] K.M. Mayer, J.H. Hafner, Localized Surface Plasmon Resonance Sensors, Chem. Rev. 111 (2011) 3828–3857.
https://doi.org/10.1021/cr100313v.
[7] C.L. Haynes, R.P. Van Duyne, Nanosphere Lithography: A Versatile Nanofabrication Tool for Studies of Size-Dependent Nanoparticle Optics, J. Phys. Chem. B. 105 (2001) 5599–5611.
https://doi.org/10.1021/jp010657m.
[8] M. Heo, H. Cho, J.-W. Jung, J.-R. Jeong, S. Park, J.Y. Kim, High-Performance Organic Optoelectronic Devices Enhanced by Surface Plasmon Resonance, Adv. Mater. 23 (2011) 5689–5693.
https://doi.org/10.1002/adma.201103753.
[9] L. Wang, R. Chen, Z.-F. Ren, C.-W. Ge, Z.-X. Liu, S.-J. He, Y.-Q. Yu, C.-Y. Wu, L.-B. Luo, Plasmonic silver nanosphere enhanced ZnSe nanoribbon/Si heterojunction optoelectronic devices, Nanotechnology. 27 (2016) 215202.
https://doi.org/10.1088/0957-4484/27/21/215202.
[10] N.C. Lindquist, C.D.L. de Albuquerque, R.G. Sobral-Filho, I. Paci, A.G. Brolo, High-speed imaging of surface-enhanced Raman scattering fluctuations from individual nanoparticles, Nat. Nanotechnol. 14 (2019) 981–987.
https://doi.org/10.1038/s41565-019-0535-6.
[11] Z. Liu, Y. Zhong, I. Shafei, R. Borman, S. Jeong, J. Chen, Y. Losovyj, X. Gao, N. Li, Y. Du, E. Sarnello, T. Li, D. Su, W. Ma, X. Ye, Tuning infrared plasmon resonances in doped metal-oxide nanocrystals through cation-exchange reactions, Nat. Commun. 10 (2019) 1394.
https://doi.org/10.1038/s41467-019-09165-2.
[12] S. Nie, S.R. Emory, Probing Single Molecules and Single Nanoparticles by Surface-Enhanced Raman Scattering, Science. 275 (1997) 1102–1106.
https://doi.org/10.1126/science.275.5303.1102.
[13] K. Ataka, S.T. Stripp, J. Heberle, Surface-enhanced infrared absorption spectroscopy (SEIRAS) to probe monolayers of membrane proteins, Biochim. Biophys. Acta BBA - Biomembr. 1828 (2013) 2283–2293.
https://doi.org/10.1016/j.bbamem.2013.04.026.
[14] Y. Kato, M. Kikugawa, E. Sudo, Attenuated Total Reflection Surface-Enhanced Infrared Absorption (ATR SEIRA) Spectroscopy for the Analysis of Fatty Acids on Silver Nanoparticles, Appl. Spectrosc. 71 (2017) 2083–2091.
https://www.osapublishing.org/as/abstract.cfm?URI=as-71-9-2083
[15] A.D. McFarland, M.A. Young, J.A. Dieringer, R.P. Van Duyne, Wavelength-scanned surface-enhanced Raman excitation spectroscopy, J. Phys. Chem. B. 109 (2005) 11279–11285.
https://doi.org/10.1021/jp050508u.
[16] Y.B. Zheng, B.K. Juluri, L.L. Jensen, D. Ahmed, M. Lu, L. Jensen, T.J. Huang, Dynamic Tuning of Plasmon–Exciton Coupling in Arrays of Nanodisk–J-aggregate Complexes, Adv. Mater. 22 (2010) 3603–3607.
https://doi.org/10.1002/adma.201000251.
[17] C. Sánchez-Aké, T. Cesca, O. Kolokoltsev, I.G. Balasa, J.A. Reyes-Esqueda, G. Mattei, Buffer-layer-assisted morphological manipulation of metal nanoparticle arrays by laser irradiation, Appl. Surf. Sci. 487 (2019) 726–733.
https://doi.org/10.1016/j.apsusc.2019.05.062.
[18] A. Kosinova, D. Wang, E. Baradács, B. Parditka, T. Kups, L. Klinger, Z. Erdélyi, P. Schaaf, E. Rabkin, Tuning the nanoscale morphology and optical properties of porous gold nanoparticles by surface passivation and annealing, Acta Mater. 127 (2017) 108–116.
https://doi.org/10.1016/j.actamat.2017.01.014.
[19] C.M. Müller, F.C.F. Mornaghini, R. Spolenak, Ordered arrays of faceted gold nanoparticles obtained by dewetting and nanosphere lithography, Nanotechnology. 19 (2008) 485306.
https://doi.org/10.1088/0957-4484/19/48/485306.
[20] H. Zhang, C. Wang, H. Li, L. Jiang, D. Men, J. Wang, J. Xiang, Physical process-aided fabrication of periodic Au–M (M = Ag, Cu, Ag–Cu) alloyed nanoparticle arrays with tunable localized surface plasmon resonance and diffraction peaks, RSC Adv. 8 (2018) 9134–9140.
https://doi.org/10.1039/C7RA13567J.
[21] N.G. Quilis, M. Lequeux, P. Venugopalan, I. Khan, W. Knoll, S. Boujday, M.L. de la Chapelle, J. Dostalek, Tunable laser interference lithography preparation of plasmonic nanoparticle arrays tailored for SERS, Nanoscale. 10 (2018) 10268–10276.
https://doi.org/10.1039/C7NR08905H.
[22] D. Chen, X. Zhang, A.F. Lee, Synthetic strategies to nanostructured photocatalysts for CO2 reduction to solar fuels and chemicals, J. Mater. Chem. A. 3 (2015) 14487–14516.
https://doi.org/10.1039/C5TA01592H.
[23] H.B. Jeon, P.V. Tsalu, J.W. Ha, Shape Effect on the Refractive Index Sensitivity at Localized Surface Plasmon Resonance Inflection Points of Single Gold Nanocubes with Vertices, Sci. Rep. 9 (2019) 13635.
https://doi.org/10.1038/s41598-019-50032-3.
[24] C.S.H. Hwang, M.-S. Ahn, Y. Lee, T. Chung, K.-H. Jeong, Ag/Au Alloyed Nanoislands for Wafer-Level Plasmonic Color Filter Arrays, Sci. Rep. 9 (2019) 9082.
https://doi.org/10.1038/s41598-019-45689-9.
[25] K.A. Willets, R.P. Van Duyne, Localized Surface Plasmon Resonance Spectroscopy and Sensing, Annu. Rev. Phys. Chem. 58 (2007) 267–297.
https://doi.org/10.1146/annurev.physchem.58.032806.104607.
[26] Y. Luo, Y. Zhou, S. Zou, J. Zhao, Dielectric domain distribution on Au nanoparticles revealed by localized surface plasmon resonance, J. Mater. Chem. C. 6 (2018) 12038–12044.
https://doi.org/10.1039/C8TC02944J.
[27] G.H. Chan, J. Zhao, G.C. Schatz, R.P. Van Duyne, Localized Surface Plasmon Resonance Spectroscopy of Triangular Aluminum Nanoparticles, J. Phys. Chem. C. 112 (2008) 13958–13963.
https://doi.org/10.1021/jp804088z.
[28] C.-Y. Chang, H.-T. Lin, M.-S. Lai, T.-Y. Shieh, C.-C. Peng, M.-H. Shih, Y.-C. Tung, Flexible Localized Surface Plasmon Resonance Sensor with Metal–Insulator–Metal Nanodisks on PDMS Substrate, Sci. Rep. 8 (2018) 11812.

https://doi.org/10.1038/s41598-018-30180-8.
[29] L. Gao, C. Ma, S. Wei, A.V. Kuklin, H. Zhang, H. Ågren, Applications of Few-Layer Nb2C MXene: Narrow-Band Photodetectors and Femtosecond Mode-Locked Fiber Lasers, ACS Nano. 15 (2021) 954–965. https://doi.org/10.1021/acsnano.0c07608.
[30] B. Guo, Q. Xiao, S. Wang, H. Zhang, 2D Layered Materials: Synthesis, Nonlinear Optical Properties, and Device Applications, Laser Photonics Rev. 13 (2019) 1800327. https://doi.org/10.1002/lpor.201800327.
[31] A. Tittl, A.-K.U. Michel, M. Schäferling, X. Yin, B. Gholipour, L. Cui, M. Wuttig, T. Taubner, F. Neubrech, H. Giessen, A Switchable Mid-Infrared Plasmonic Perfect Absorber with Multispectral Thermal Imaging Capability, Adv. Mater. 27 (2015) 4597–4603. https://doi.org/10.1002/adma.201502023.
[32] Z. Liao, Z. Liu, Y. Wang, X. Liu, G. Liu, Ultra-narrowband resonant light absorber for high-performance thermal-optical modulators, Opt. Express. 29 (2021) 31048–31057. https://doi.org/10.1364/OE.439107.
[33] M. Gaudin, P. Carles, E. Laborde, C. Champeaux, F. Dumas-Bouchiat, A dual nanosecond-pulsed laser setup for nanocomposite synthesis—Ag nanoparticles in Al2O3/VO2 matrix, J. Appl. Phys. 125 (2019) 054301.
https://doi.org/10.1063/1.5058107.
[34] J.A. Ramirez-Rincon, C.L. Gomez-Heredia, A. Corvisier, J. Ordonez-Miranda, T. Girardeau, F. Paumier, C. Champeaux, F. Dumas-Bouchiat, Y. Ezzahri, K. Joulain, O. Ares, J.J. Alvarado-Gil, Thermal hysteresis measurement of the VO_2 dielectric function for its metal-insulator transition by visible-IR ellipsometry, J. Appl. Phys. 124 (2018) 195102.
[35] A. La Rosa, M. Yan, R. Fernandez, E. Zegarra, Proton-Fountain Electric-Field-Assisted Nanolithography (PEN): Fabrication of Polymer Nanostructures that Respond to Chemical and Electrical Stimuli. An Overview in the Context of the Top-Down and Bottom-Up Approaches to Nanotechnology, REVCIUNI. (2012).
https://pdxscholar.library.pdx.edu/phy_fac/183.
[36] L. Bruchhaus, P. Mazarov, L. Bischoff, J. Gierak, A.D. Wieck, H. Hövel, Comparison of technologies for nano device prototyping with a special focus on ion beams: A review: Appl. Phys. Rev. 4 (2017) 011302
https://doi.org/10.1063/1.4972262.
[37] A.I. Bercea, C. Champeaux, C.D. Constantinescu, F. Dumas-Bouchiat, Vanadium dioxide-iridium composite development: specific near infrared surface plasmon resonance, J. Compos. Sci. 5 (2021), 193.
https://doi.org/10.3390/jcs5070193.
[38] W. Yu, Y. Lu, X. Chen, H. Xu, J. Shao, X. Chen, Y. Sun, J. Hao, N. Dai, Large-Area, Broadband, Wide-Angle Plasmonic Metasurface Absorber for Midwavelength Infrared Atmospheric Transparency Window, Adv. Opt. Mater. 7 (2019) 1900841. https://doi.org/10.1002/adom.201900841.
https://doi.org/10.1063/1.5049747.
[39] U.Ch. Fischer, H.P. Zingsheim, Submicroscopic pattern replication with visible light, J. Vac. Sci. Technol. 19 (1981) 881–885.
https://doi.org/10.1116/1.571227.
[40] Ph. Buffat, J.-P. Borel, Size effect on the melting temperature of gold particles, Phys. Rev. A. 13 (1976) 2287–2298.
https://doi.org/10.1103/PhysRevA.13.2287.
[41] C. Zhao, Y. Zhu, Y. Su, Z. Guan, A. Chen, X. Ji, X. Gui, R. Xiang, Z. Tang, Tailoring Plasmon Resonances in Aluminium Nanoparticle Arrays Fabricated Using Anodic Aluminium Oxide, Adv. Opt. Mater. 3 (2015) 248–256.
https://doi.org/10.1002/adom.201400325.
[42] Z. Qiao, H. Feng, J. Zhou, Molecular dynamics simulations on the melting of gold nanoparticles, Phase Transit. 87 (2014) 59–70.
https://doi.org/10.1080/01411594.2013.798410.
[43] G.L. Allen, R.A. Bayles, W.W. Gile, W.A. Jesser, Small particle melting of pure metals, Thin Solid Films. 144 (1986) 297–308.
https://doi.org/10.1016/0040-6090(86)90422-0.
[44] Y. Fang, C. Wang, H. Jiang, Crystallization of self-propelled particles on a spherical substrate, Appl. Math. Mech. 40 (2019) 1387–1398.
https://doi.org/10.1007/s10483-019-2525-8.
[45] S.K. Gupta, M. Talati, P.K. Jha, Shape and Size Dependent Melting Point Temperature of Nanoparticles, Mater. Sci. Forum. (2008).
https://doi.org/10.4028/www.scientific.net/MSF.570.132.
[46] P. Antoniammal, D. Arivuoli, Size and Shape Dependence on Melting Temperature of Gallium Nitride Nanoparticles, J. Nanomater. (2012).
https://doi.org/10.1155/2012/415797.
[47] C.V. Thompson, Solid-State Dewetting of Thin Films, Annu. Rev. Mater. Res. 42 (2012) 399–434.
https://doi.org/10.1146/annurev-matsci-070511-155048.
[48] P. Farzinpour, A. Sundar, K.D. Gilroy, Z.E. Eskin, R.A. Hughes, S. Neretina, Altering the dewetting characteristics of ultrathin gold and silver films using a sacrificial antimony layer, Nanotechnology. 23 (2012) 495604.
https://doi.org/10.1088/0957-4484/23/49/495604.
[49] L.W. Martin, Y.-H. Chu, R. Ramesh, Advances in the growth and characterization of magnetic, ferroelectric, and multiferroic oxide thin films, Mater. Sci. Eng. R Rep. 68 (2010) 89–133.
https://doi.org/10.1016/j.mser.2010.03.001.
[50] N. Masoud, T. Partsch, K.P. de Jong, P.E. de Jongh, Thermal stability of oxide-supported gold nanoparticles, GOLD Bull. (2019).
https://doi.org/10.1007/s13404-019-00259-9.
[51] D. Chatterjee, A. R, K. Kamalnath, R. Ahmad, A.K. Singh, N. Ravishankar, Orientation Selection during Heterogeneous Nucleation: Implications for Heterogeneous Catalysis, J. Phys. Chem. C. 121 (2017) 10027–10037.
https://doi.org/10.1021/acs.jpcc.7b02237.
[52] E.J. Siem, W.C. Carter ‡, D. Chatain §, The equilibrium shape of anisotropic interfacial particles, Philos. Mag. 84 (2004) 991–1010.
https://doi.org/10.1080/14786430310001639897.
[53] E.D. Palik, Handbook of optical constants of solids, Academic Press, Orlando, 1985.
https://doi.org/10.1016/C2009-0-20920-2.
[54] R.L. Olmon, B. Slovick, T.W. Johnson, D. Shelton, S.-H. Oh, G.D. Boreman, M.B. Raschke, Optical dielectric function of gold, Phys. Rev. B. 86 (2012) 235147.
https://doi.org/10.1103/PhysRevB.86.235147.
[55] V. Théry, A. Boulle, A. Crunteanu, J.C. Orlianges, A. Beaumont, R. Mayet, A. Mennai, F. Cosset, A. Bessaudou, M. Fabert, Role of thermal strain in the metal-insulator and structural phase transition of epitaxial ${\mathrm{VO}}_{2}$ films, Phys. Rev. B. 93 (2016) 184106.
https://doi.org/10.1103/PhysRevB.93.184106.
[56] M. Yang, Y. Yang, B. Hong, L. Wang, Z. Luo, X. Li, C. Kang, M. Li, H. Zong, C. Gao, Surface-growth-mode-induced strain effects on the metal–insulator transition in epitaxial vanadium dioxide thin films, RSC Adv. 5 (2015) 80122–80128.
https://doi.org/10.1039/C5RA13490K.
[57] H. Matsui, Y.-L. Ho, T. Kanki, H. Tanaka, J.-J. Delaunay, H. Tabata, Mid-infrared Plasmonic Resonances in 2D VO2 Nanosquare Arrays, Adv. Opt. Mater. 3 (2015) 1759–1767.
https://doi.org/10.1002/adom.201500322.
[58] D.W. Ferrara, J. Nag, E.R. MacQuarrie, A.B. Kaye, R.F. Haglund, Plasmonic probe of the semiconductor to metal phase transition in vanadium dioxide, Nano Lett. 13 (2013), 4169.
https://doi.org/10.1021/nl401823r
[59] L. Zhao, K.L. Kelly, G.C. Schatz, The Extinction Spectra of Silver Nanoparticle Arrays: Influence of Array Structure on Plasmon Resonance Wavelength and Width, J. Phys. Chem. B. 107 (2003) 7343–7350.
https://doi.org/10.1021/jp034235j.

[60] K. Appavoo, D.Y. Lei, Y. Sonnefraud, B. Wang, S.T. Pantelides, S.A. Maier, R.F. Haglund, Role of Defects in the Phase Transition of VO2 Nanoparticles Probed by Plasmon Resonance Spectroscopy, Nano Lett. 12 (2012) 780–786.
https://doi.org/10.1021/nl203782y.
[61] P. Zhang, K. Jiang, Q. Deng, Q. You, J. Zhang, J. Wu, Z. Hu, J. Chu, Manipulations from oxygen partial pressure on the higher energy electronic transition and dielectric function of VO2 films during a metal–insulator transition process, J. Mater. Chem. C. 3 (2015) 5033–5040.
https://doi.org/10.1039/C5TC00002E.
[62] Hiroaki Matsui, Femtosecond Imaging - Chapter: Surface Plasmons and Optical Dynamics on Vanadium Dioxide | IntechOpen (2020)
https://doi.org/10.5772/intechopen.91215
[63] P. Shvets, O. Dikaya, K. Maksimova, A. Goikhman, A review of Raman spectroscopy of vanadium oxides, J. Raman Spectrosc. 50 (2019) 1226–1244.
https://doi.org/10.1002/jrs.5616.
[64] S.S. Majid, D.K. Shukla, F. Rahman, S. Khan, K. Gautam, A. Ahad, S. Francoual, R.J. Choudhary, V.G. Sathe, J. Strempfer, Insulator-metal transitions in the T phase Cr-doped and $M1$ phase undoped ${\mathrm{VO}}_{2}$ thin films, Phys. Rev. B. 98 (2018) 075152.
https://doi.org/10.1103/PhysRevB.98.075152.
[65] B.T. O'Callahan, A.C. Jones, J. Hyung Park, D.H. Cobden, J.M. Atkin, M.B. Raschke, Inhomogeneity of the ultrafast insulator-to-metal transition dynamics of VO2, Nat. Commun. 6 (2015) 6849.
https://doi.org/10.1038/ncomms7849.
[66] A.M. Makarevich, I.I. Sadykov, D.I. Sharovarov, V.A. Amelichev, A.A. Adamenkov, D.M. Tsymbarenko, A.V. Plokhih, M.N. Esaulkov, P.M. Solyankin, A.R. Kaul, Chemical synthesis of high-quality epitaxial vanadium dioxide films with sharp electrical and optical switch properties, J. Mater. Chem. C. 3 (2015) 9197–9205.
https://doi.org/10.1039/C5TC01811K.
[67] H. Zhang, Q. Li, P. Shen, Q. Dong, B. Liu, R. Liu, T. Cui, B. Liu, The structural phase transition process of free-standing monoclinic vanadium dioxide micron-sized rods: temperature-dependent Raman study, RSC Adv. 5 (2015) 83139–83143.
https://doi.org/10.1039/C5RA15947D.
[68] D.H. Jung, H.S. So, K.H. Ko, J.W. Park, H. Lee, T.T.T. Nguyen, S. Yoon, Electrical and optical properties of VO2 thin films grown on various sapphire substrates by using RF sputtering deposition, J. KOREAN Phys. Soc. 69 (2016) 1787.
https://doi.org/10.3938/jkps.69.1787